Draft version July 26, 2019
Preprint typeset using LaTeX style emulateapj v. 12/16/11

SPECTROSCOPIC CONFIRMATION OF A COMA CLUSTER PROGENITOR AT $z \sim 2.2$

Behnam Darvish[1], Nick Z. Scoville[1], Christopher Martin[1], David Sobral[2], Bahram Mobasher[3], Alessandro Rettura[4], Jorryt Matthee[5], Peter Capak[6], Nima Chartab[3], Shoubaneh Hemmati[4], Daniel Masters[4], Hooshang Nayyeri[7], Donal O'Sullivan[1], Ana Paulino-Afonso[8], Zahra Sattari[3], Abtin Shahidi[3], and Mara Salvato[8]

Draft version July 26, 2019

ABSTRACT

We report the spectroscopic confirmation of a new protocluster in the COSMOS field at $z \sim 2.2$, originally identified as an overdensity of narrow-band selected Hα emitting candidates. With only two masks of Keck/MOSFIRE near-IR spectroscopy in both H ($\sim$ 1.47-1.81 μm) and K ($\sim$ 1.92-2.40 μm) bands ($\sim$ 1.5 hour each), we confirm 35 unique protocluster members with at least two emission lines detected with S/N $>$ 3. Combined with 12 extra members from the zCOSMOS-deep spectroscopic survey (47 in total), we estimate a mean redshift, line-of-sight velocity dispersion, and total mass of z_{mean}=2.23224 $\pm$ 0.00101, σ_{los}=645 $\pm$ 69 km s^{-1}, and $M_{vir} \sim (1-2)\times10^{14}$ $M_{\odot}$ for this protocluster, respectively. We estimate a number density enhancement of $\delta_g \sim 7$ for this system and we argue that the structure is likely not virialized at $z \sim 2.2$. However, in a spherical collapse model, δ_g is expected to grow to a linear matter enhancement of ~ 1.9 by z=0, exceeding the collapse threshold of 1.69, and leading to a fully collapsed and virialized Coma-type structure with a total mass of $M_{dyn}(z{=}0) \sim 9.2\times10^{14}$ $M_{\odot}$ by now. This observationally efficient confirmation suggests that large narrow-band emission-line galaxy surveys, when combined with ancillary photometric data, can be used to effectively trace the large-scale structure and protoclusters at a time when they are mostly dominated by star-forming galaxies.

Subject headings: galaxies: clusters: general — galaxies: groups: general — galaxies: high-redshift — galaxies: evolution — galaxies: star formation — large-scale structure of universe

1. INTRODUCTION

Galaxy clusters and protoclusters at high redshifts ($z \gtrsim 2$) are ideal laboratories for studying structure formation, cosmology, and the effect of early environments on galaxy formation and evolution. The latter is particularly important as the $z \sim$ 2-3 redshift regime traces the peak of star-formation and AGN activity in the universe (Madau & Dickinson 2014; Khostovan et al. 2015), when many physical processes, such as cold gas flow into galaxies, outflow and feedback processes, mergers, and likely environment governed the evolution of galaxies.

At low redshift, the relation between galaxy properties and environment is relatively well established. However, at high redshifts ($z \gtrsim 2$), there are conflicting results, partly due to the small number of confirmed structures, and often having only a small number of confirmed members.

At $z \gtrsim 2$, there is poor agreement between current studies on the mass-metallicity relation, with results varying from an absence of any environmental trends (Kacprzak et al. 2015), to an enhancement (Shimakawa et al. 2015), or a deficiency of metals (Valentino et al. 2015) for star-forming galaxies in denser environments. The situation is the same regarding the relation between environment and star-formation activity in galaxies at $z \gtrsim 2$ (e.g.; see Darvish et al. 2016 vs. Shimakawa et al. 2018) and the environmental dependence of the gas content of galaxies (e.g.; see Noble et al. 2017; Lee et al. 2017; Darvish et al. 2018; Hayashi et al. 2018). The discrepant results are likely caused by different dynamical state of the environments probed, different selection functions, small sample sizes, AGN contamination, different star formation rate (SFR), metallicity, and gas mass indicators used, complications due to extinction correction and so on. This implies the need for finding more high-z structures with well-defined sample of galaxies and a large number of confirmed spectroscopic measurements.

Cluster candidates at high redshifts can be detected through the concentration of quiescent galaxies (e.g.; Strazzullo et al. 2015), by probing the environment of highly rare and active systems, such as quasars, radio and sub-mm galaxies, and Lyα blobs (e.g.; Matsuda et al. 2004; Venemans et al. 2007; Capak et al. 2011; Wylezalek et al. 2013), or an overdensity of IR sources with e.g. *Spitzer*, *Herschel*, or *Planck* (e.g.; Muzzin et al. 2013; Rettura et al. 2014; Clements et al. 2014). These approaches have led to the spectroscopic confirmation of a number of candidate structures at $z \gtrsim 2$ (e.g.; Capak et al. 2011; Yuan et al. 2014; Lemaux et al. 2014; Cucciati et al. 2014, 2018; also see the review by Overzier 2016). The detection and spectroscopic confirmation of clusters traced by passive galaxies is hard because of the small

[1] Cahill Center for Astrophysics, California Institute of Technology, 1216 East California Boulevard, Pasadena, CA 91125, USA; email: bdarv@caltech.edu; bdarv001@ucr.edu
[2] Department of Physics, Lancaster University, Lancaster, LA1 4YB, UK
[3] Department of Physics and Astronomy, University of California, Riverside, 900 University Ave, Riverside, CA 92521, USA
[4] Jet Propulsion Laboratory, California Institute of Technology, 4800 Oak Grove Drive, Pasadena, CA 91109, USA
[5] Department of Physics, ETH Zürich, Wolfgang-Pauli-Strasse 27, CH-8093 Zürich, Switzerland
[6] IPAC, Mail Code 314-6, California Institute of Technology, 1200 East California Boulevard, Pasadena, CA 91125, USA
[7] Department of Physics and Astronomy, University of California Irvine, Irvine, CA 92697, USA
[8] Max-Planck-Institut für extraterrestrische Physik (MPE), Giessenbachstrasse 1, D-85748 Garching bei München, Germany

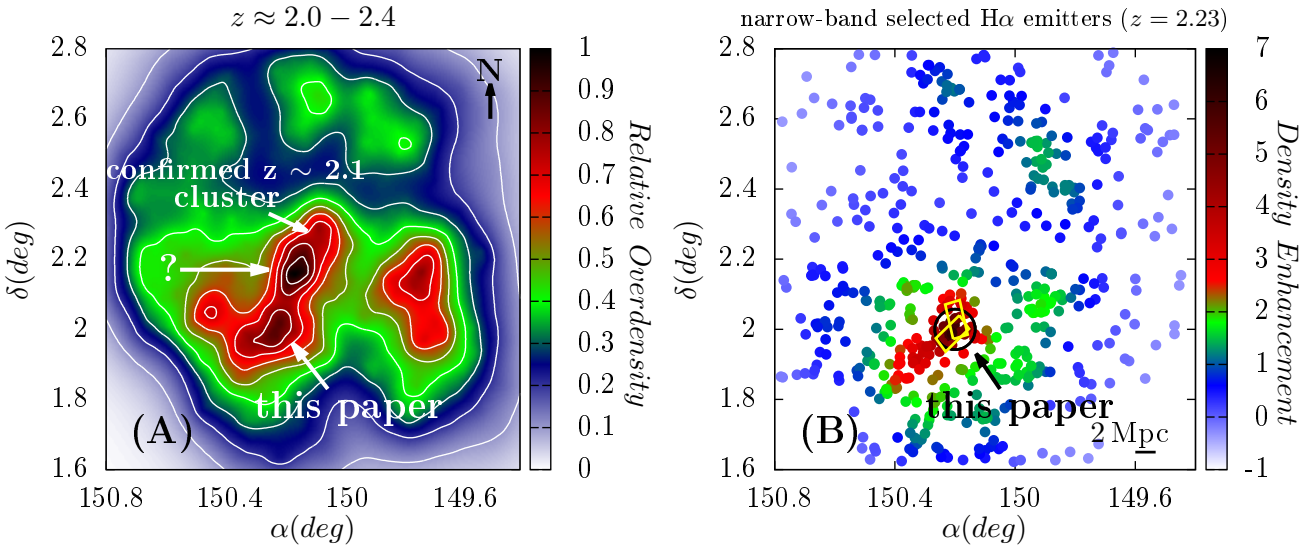

FIG. 1.— Left panel — (A) Relative overdensity map in the COSMOS field for a redshift slice centered at z=2.23 (redshift width of $\approx \pm$ 0.2). The map is adaptively smoothed using a weighted adaptive Gaussian Kernel (Darvish et al. 2015, 2017) with a global kernel width of 2 Mpc. An extended, several Mpc-scale LSS is clearly seen. The northern section of this LSS is a spectroscopically confirmed cluster at $z \sim 2.1$ (Yuan et al. 2014). There is evidence for some overdensity in the middle section of this structure (shown with a question mark). There is also an extended southern section to this structure. Right panel — (B) Spatial distribution of narrow-band selected Hα emitter candidates from the HiZELS/COSMOS survey (Sobral et al. 2013) at $z \sim 2.23$ (redshift width of $\sim$ 0.03-0.04) color-coded by their density enhancement. The southern section of the extended LSS (left panel) is clearly seen as an overdensity of narrow-band selected Hα emitting candidates. We perform follow-up spectroscopic observations targeting the densest region of this southern section shown with a black circle of 2 Mpc radius. The positions of the spectroscopic masks (Section 3.2) are shown with yellow rectangles. Note the $z \sim 2.1$ cluster and the potential central overdensity (shown with the question mark on the left panel) are not seen here given the narrowness of the narrow-band filter.

number density of quiescent galaxies at higher reshifts and the lack of emission lines in their spectra which makes the spectroscopic observations challenging. Moreover, the rarity of very active galaxies such as quasars in the present day surveys makes the high-z protocluster detection probed by them difficult.

An observationally efficient and physically motivated technique to identify protoclusters at $z \gtrsim 2$ is to target concentrations of emission-line galaxies, such as Hα and Lyα emitters using narrow-band filters (e.g.; Matsuda et al. 2011; Koyama et al. 2013). The high concentration of star-forming, emission-line systems (prior to quenching) in protoclusters has been theoretically predicted by the hierarchical galaxy formation models and has successfully resulted in the spectroscopic confirmation of some protoclusters and large-scale structures (LSSs) at $z \gtrsim 2$ (e.g.; Chiang et al. 2015; Lemaux et al. 2018). Therefore, large emission-line galaxy surveys can be used to effectively trace the LSSs and protoclusters at $z \gtrsim 2$.

Here, we report the spectroscopic confirmation of a protocluster, originally found as an overdensity of narrow-band selected Hα emitters at $z \sim 2.2$ in the High-Z Emission Line Survey (HiZELS) (Geach et al. 2012; Sobral et al. 2013, 2014) of the Cosmic Evolution Survey (COSMOS) field (Scoville et al. 2007). In Section 2, we explain the protocluster selection. In Section 3, we present the spectroscopic observations and equip them with ancillary spectroscopic data. The protocluster properties and its fate are presented in Section 4. The results are compared with other high-z protoclusters in Section 5. We summarize the results in Section 6.

Throughout this letter, we assume a flat ΛCDM cosmology with H_0=70 km s^{-1} Mpc^{-1}, Ω_m=0.3, and Ω_Λ=0.7. Unless otherwise stated, the transverse cosmological distances are presented as physical distances. The "physical" scale at the redshift of the protocluster ($z \sim$ 2.23) is $\sim$ 0.5 Mpc per arcmin.

2. PROTOCLUSTER SELECTION

Figure 1 (A) shows the relative overdensity map in the COSMOS field for a redshift slice centered at z=2.23, with a width $\pm 1.5\sigma_{\Delta z/(1+z)} \approx \pm$ 0.2 from the center of the slice (Darvish et al. 2017), where $\sigma_{\Delta z/(1+z)}$ is the typical photometric redshift uncertainty at $z \sim 2.2$ (Laigle et al. 2016). In making this map, all galaxies more massive than the mass completeness limit ($\geqslant 10^{10}$ $M_\odot$) at this redshift are selected. In addition, $\geqslant$ 90% of the photometric redshift probability distribution function of these galaxies should lie within the boundaries of this redshift slice. The map is adaptively smoothed using a weighted adaptive Gaussian Kernel (Darvish et al. 2015) with a global kernel width of 2 Mpc. An extended, several Mpc-scale LSS is clearly seen. The northern section of this LSS is a spectroscopically confirmed cluster at $z \sim 2.1$ (Yuan et al. 2014). There is evidence for some conspicuous overdensity in the middle section of this structure. There is also an extended southern section to this structure which is the focus of this paper.

Figure 1 (B) clearly reveals this southern section. Here, we show the spatial distribution of uniformly-probed narrow-band selected Hα emitter candidates from the HiZELS survey (Sobral et al. 2013) in the COSMOS field at $z \sim 2.23$ (Section 3.1). They are color-coded by their density enhancement defined as $\frac{\Sigma-\Sigma_0}{\Sigma_0}$, where Σ is the surface number density and Σ_0 is the mean surface number density. This southern section stands out as an overdensity of Hα emitters (see also Geach et al. 2012). We perform follow-up spectroscopic observations with Keck/MOSFIRE targeting the densest region of this

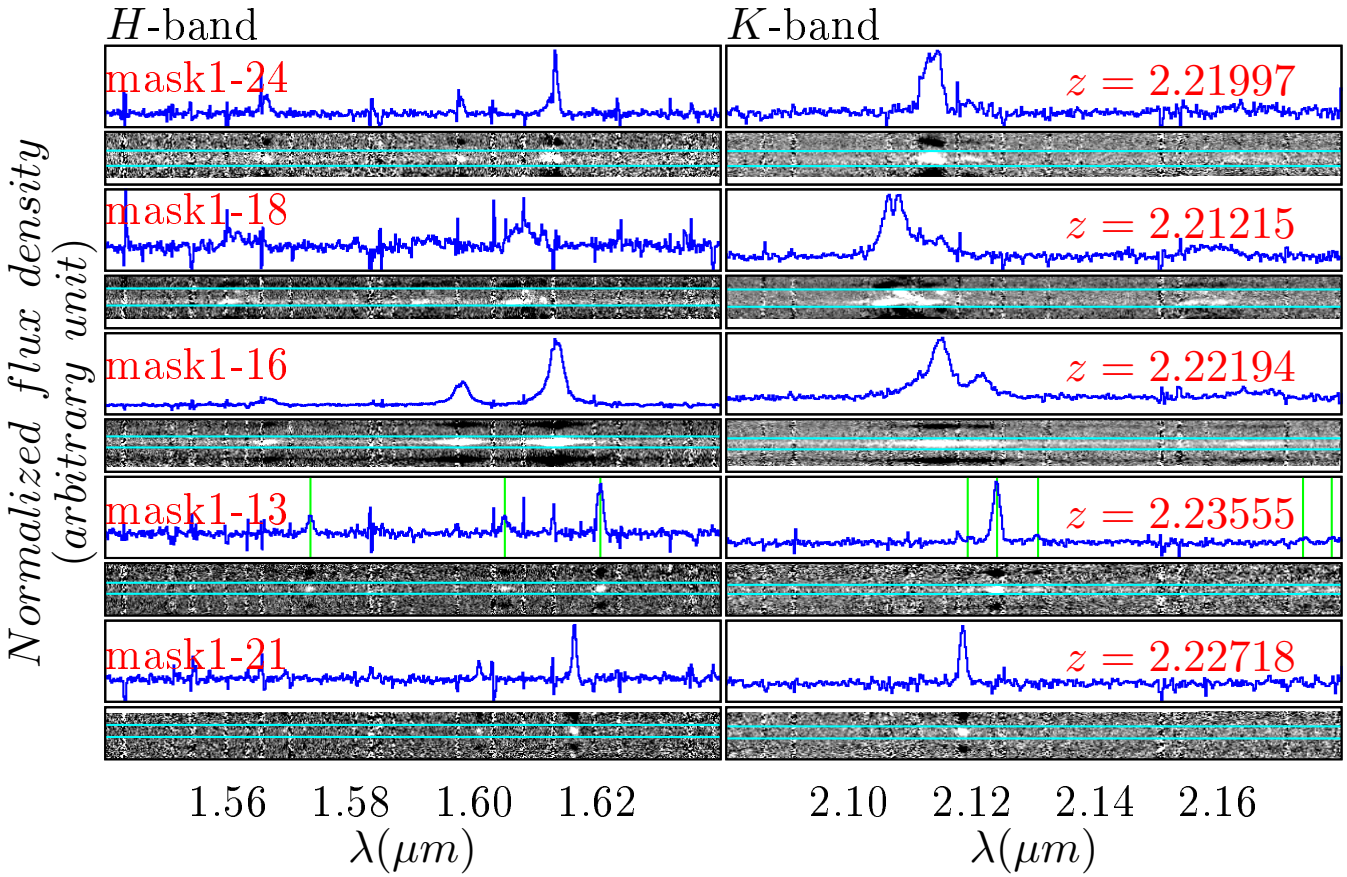

FIG. 2.— Example 2D and extracted 1D spectra showing some emission lines. Cyan lines show the 1D extraction window. The position of Hβ, [OIII]λ4959, [OIII]λ5007, [NII]λ6549, Hα, [NII]λ6583, [SII]λ6717, and [SII]λ6731 emission lines is shown with vertical green lines for one of the galaxies. The top two spectra show two merger cases, the third one is a broad-line AGN, and the last two spectra show normal star-forming galaxies in the protocluster.

southern section as a potential protocluster (shown with a black circle in Figure 1 (B)).

3. SPECTROSCOPIC OBSERVATIONS

3.1. *Sample Selection for Spectroscopy*

To increase the success rate of our spectroscopic observations, we focus on potential targets in the vicinity of the candidate protocluster that are likely emission-line galaxies (e.g.; star-forming, starburst or AGN). This is because detecting emission lines is easier and observationally more efficient than finding absorption features in the stellar continuum which require longer integration times. Moreover, the strongest absorption features appear around the rest-frame 4000 Å which are then redshifted to the J band at the presumed redshift of the protocluster, a region populated by many atmospheric absorption and emission features.

Hence, as the primary targets in the vicinity of the overdensity, we rely on the narrow-band selected Hα emitting candidates from the HiZELS survey (Sobral et al. 2013) in the COSMOS field at $z \sim 2.23$. These are detected as excess color in the UKIRT/WFCAM and VLT/HAWK-I narrow-band K filters (centered at $\lambda \sim$ 2.12-2.13 μm with a FWHM $\Delta\lambda \sim$ 200-300 Å, corresponding to a redshift width of $\Delta z \sim$ 0.03-0.04 centered at $z \sim$ 2.23-2.24) relative to the broad-band K filter. To minimize contamination from other emission lines, if available, a combination of double-line detections (in both narrow-band K and H and/or K and J), broad-band color-color selections ($Z-K$ vs. $B-Z$ and $B-R$ vs. $U-B$), and photometric redshift cuts ($1.7 < z_{phot} < 2.8$) were also implemented. This primary target list is complete down to an Hα flux of $\gtrsim 1\times10^{-17}$ erg s^{-1}cm^{-2}, rest-frame EW(Hα+[NII]) $\geqslant$ 25 Å, observed SFR $\gtrsim 3\ M_{\odot}yr^{-1}$ (Chabrier initial mass function), and stellar mass limits of $\gtrsim 10^{9.7}\ M_{\odot}$ (see Sobral et al. 2013, 2014 for details).

In our design of the multi-object spectroscopic masks, we also added filler objects. They are selected from either the latest COSMOS2015 K_s-band selected or the previous I-band selected photometric redshift catalogs (Laigle et al. 2016; Ilbert et al. 2009). The fillers are selected to be in the vicinity of the overdensity, classified as star-forming galaxies (to increase their detection rate) based on their rest-frame $NUV-r$ vs. $r-J$ colors (Ilbert et al. 2013), with their photometric redshift in the range $1.7 < z_{phot} < 2.8$. Given their selection, some of the fillers may belong to the potential protocluster as well.

3.2. *Observational Strategy*

The observations were conducted on December 8, 2018 and January 13-15, 2019 with KeckI/MOSFIRE NIR multi-object spectrograph under clear conditions with the average seeing of $\sim 0.5''$-$0.6''$ in December and $\sim$

TABLE 1
Coordinate and Redshift of the Sources

Number	RA (deg)	Dec (deg)	spectroscopic z	ID(HiZELS)	ID(COSMOS)[a]	K_s(COSMOS) mag	comment
mask1-1	150.184235	2.035242	2.23227	S12B-1073	483880	21.053	primary
mask1-2	150.162308	1.999728	2.23796	S12B-1133	461469	21.780	primary
mask1-3	150.162231	1.997168	2.23962	S12B-1142	459801	22.225	primary
mask1-4	150.178958	2.009019	-	-	465362	16.753	2MASS star
mask1-5	150.197937	2.026497	2.23767	S12B-1089	478717	22.143	primary
mask1-51	150.200721	2.023885	2.23675	-	476338	23.899	serendipitous
mask1-6*	150.179947	1.992562	2.23276	S12B-1149	457031	23.414	primary
mask1-7	150.201492	2.011835	2.22076	S12B-1115	469074	22.781	primary
mask1-8	150.207275	2.015360	2.22390	S12B-1110	471600	21.757	primary, merger?
mask1-81	150.208559	2.014025	2.24683	-	470941	22.171	serendipitous
mask1-9	150.214371	2.013219	2.23730	S12B-1111	470543	21.507	primary
mask1-91*	150.213577	2.014169	2.23653	S12B-1108	470634	22.683	serendipitous
mask1-10	150.208500	2.002617	2.04398	-	463455	22.508	filler, field
mask1-11	150.215375	2.004858	2.21980	-	464709	23.769	filler
mask1-12	150.210208	1.995008	2.99093	-	-	-	filler, field
mask1-13	150.208420	1.989571	2.23555	S12B-9026	455052	22.451	primary
mask1-14	150.209686	1.983837	2.23588	S12B-9096	451484	22.204	primary, merger
mask1-15	150.216417	1.988758	2.22850	-	455603	20.372	filler
mask1-16	150.230774	1.998720	2.22194	S12B-1139	462238	21.365	primary
mask1-17	150.218689	1.981452	2.23929	S12B-9145	450967	22.385	primary
mask1-18	150.217958	1.969297	2.21215	-	443583	20.477	filler, triple merger?
mask1-19	150.235428	1.984851	2.22909	S12B-9103	452250	22.433	primary
mask1-20	150.227844	1.954604	2.22964	S12B-9563	433445	22.825	primary
mask1-21	150.252487	1.980309	2.22718	S12B-9161	449433	23.109	primary
mask1-22	150.242096	1.963336	2.24096	S12B-9425	439360	22.871	primary
mask1-23	150.247604	1.963640	2.24408	S12B-9419	439051	23.362	primary
mask1-24	150.262009	1.974060	2.21997	S12B-9256	446347	21.155	primary, merger
mask2-1	150.226868	2.069255	-	S12B-3033	506226	22.186	primary
mask2-2	150.183044	2.077852	2.23340	S12B-3052	511651	21.499	primary
mask2-3	150.224152	2.055650	2.22964	S12B-1036	496918	21.971	primary
mask2-4	150.214042	2.046742	-	-	491994	22.396	filler
mask2-5	150.178958	2.009019	-	-	465362	16.753	2MASS star
mask2-6	150.194167	2.038033	2.11461	-	485225	23.099	filler, field
mask2-7	150.199921	2.031268	2.23029	S12B-1080	481208	23.040	primary
mask2-8	150.214966	2.021282	2.23626	S12B-1097	475366	21.447	primary, merger
mask2-9	150.213974	2.019010	2.23866	S12B-1105	473829	22.526	primary, merger
mask2-10*	150.213577	2.014169	2.23653	S12B-1108	470634	22.683	primary
mask2-11	150.214042	2.046742	-	-	467174	23.073	filler
mask2-12	150.209702	1.990308	2.23784	S12B-9015	455204	23.440	primary
mask2-13	150.163498	2.000660	2.23259	S12B-1138	461703	23.766	primary
mask2-14*	150.179947	1.992562	2.23243	S12B-1149	457031	23.414	primary
mask2-15	150.207657	1.981512	2.22801	S12B-9144	450160	22.865	primary, merger?
mask2-16	150.199478	1.979534	2.23906	S12B-9175	449105	22.216	primary
mask2-17	150.168716	1.985868	2.23499	S12B-9080	454336	20.690	primary
mask2-18	150.171083	1.982756	2.23571	-	451149	21.578	filler
zDEEP-404985	150.129107	1.990073	2.2252	-	455565	22.460	ancillary
zDEEP-426887	150.130297	2.009929	2.2371	-	467708	23.504	ancillary
zDEEP-404921	150.134173	1.985729	2.2412	S12B-9081	452539	23.006	ancillary
zDEEP-427277	150.141604	2.046844	2.2328	S12B-1053	490796	23.362	ancillary
zDEEP-405266	150.146074	2.006951	2.2351	S12B-1120	465895	23.224	ancillary
zDEEP-404838	150.161394	1.981538	2.2311	-	450533	22.327	ancillary
zDEEP-418470	150.164187	1.982856	2.2239	-	451562	22.958	ancillary
zDEEP-426933	150.166506	2.014942	2.2340	-	471112	23.597	ancillary
zDEEP-427537	150.178728	2.069249	2.2269	S12B-3032	505282	24.327	ancillary
zDEEP-426643	150.209795	1.986637	2.2310	S12B-9070	453251	23.086	ancillary
zDEEP-405942	150.214480	2.044393	2.2298	-	490170	22.578	ancillary
zDEEP-418791	150.232958	2.025177	2.2245	-	477167	23.677	ancillary

[a]COSMOS IDs and K_s magnitudes are from Laigle et al. 2016 catalog.

0.3″-0.4″ in January. Given the expected redshift of the structure, we perform observations in both K ($\sim$ 1.92-2.40 μm) and H ($\sim$ 1.47-1.81 μm) bands to cover emission lines that can later be used to measure the SFR (Hα or Hβ), nebular extinction (Hβ and Hα), gas-phase metallicity ([NII]λ6549, [NII]λ6583, and Hα), electron density ([SII]$\lambda\lambda$6717,6731 doublet), source of ionization (BPT diagram), and ionization state of the gas ([OIII]λ4959, [OIII]λ5007, and Hβ) for galaxies.

We designed two masks in the vicinity of the protocluster candidate (Figure 1). They were designed in such a way to maximize the number of primary targets. The masks contained unique sources except for one source that would later be used to estimate systematics. In total, we placed 30 unique primary targets and 9 fillers on the masks.

A 2MASS star per mask was used to estimate the observing conditions, such as the seeing and the spatial profile of point sources. Using an ABBA dithering pattern, we observed each mask in each filter for a total exposure time of $\sim$ 72 to 96 minutes with a midpoint airmass of $\sim$ 1.0 to 1.3. Using sky lines, we estimate a FWHM observed spectral resolution of $\sim$ 4.5 Å and $\sim$ 6 Å in H and K bands, respectively, with the slit width of 0.7″. These correspond to $R \sim 3600$ and $\delta z \sim 0.0003$.

3.3. *Data Reduction*

We used the MOSFIRE DRP to reduce the data. The reduction involves flat fielding, cosmic-ray removal, sky subtraction, and vacuum wavelength calibration on a slit-by-slit basis. The outputs are the 2D spectra and their uncertainties. We extract the 1D spectrum and its associated error using the optimal extraction algorithm of Horne (1986). This is done by weighted summing of fluxes in an optimized window around the 2D spectrum, where the weights incorporate both the flux uncertainties and the spatial extent of the 2D spectrum (spatial profile). To determine the optimized window, we use the spatial profile of each source. To extract the spatial profile, we collapse the 2D spectrum of each source along the wavelength direction in the vicinity of bright, high S/N features and then fit a Gaussian function to the profile. We choose the optimized window as $\pm 3 \times$ the standard deviation of the spatial profile around its center. If determining the spatial profile fails because of e.g.; faint, low S/N spectrum, we instead rely on the spatial profile of our 2MASS star. In a few cases (e.g.; nearby merging systems) where determining the optimized window is tricky, we instead extract the 1D spectra in a boxcar window wide enough to fully cover all the features (e.g.; Fig. 2 second example). Finally, for all the sources, we visually check the extraction window to make sure that the fluxes are fully measured. Figure 2 shows some example 2D and their extracted 1D spectra.

3.4. *Redshift Estimation*

Table 1 lists the extracted redshifts for our spectroscopic sample in the two masks, as well as the coordinate, HiZELS ID (for primary sources), K_s magnitude, the COSMOS ID of each source (based on a match with the COSMOS2015 catalog with a 1″ radius), and whether a source is a primary target, a filler, a serendipitous detection, a potential merger, or a field galaxy. We report a secure redshift for galaxies that have at least two significant (S/N $\geqslant$ 3) emission lines. The reported redshift is the average redshift that we obtain based on the peak of all the available emission lines for each source (mostly Hα and [OIII]λ5007). For sources that show signs of mergers in their spectra and/or in their images (commented as "merger" in Table 1), the average redshift of different components is given.

To check for systematics in redshifts for objects on different masks, one object is observed twice (mask1-6* and mask2-14*). The extracted redshift difference for this source is ~ 0.0003, similar to the resolution of $\delta z \sim 0.0003$. Another primary object is also observed twice, with a serendipitous detection in the other mask (mask2-10* and mask1-91*). The extracted redshift difference for this source is zero. To check for systematics in obtaining redshifts in different bands (H and K), we compare redshifts obtained based on emission lines in each individual band (if available). The absolute difference is in the range $\Delta z(HK)$=0.00009-0.00218 with a median value of 0.00029, similar to the redshift resolution of $\delta z \sim 0.0003$. To further check the reliability of redshifts, for objects whose emission lines can be fitted with a single Gaussian function, we also determine redshift by fitting a Gaussian. In all cases, the extracted redshifts are within ~ 0.0003 of what we originally determined.

Out of 30 unique primary targets (commented as "primary" in Table 1), 29 yield secure redshifts at $z \sim 2.23$, showing the robustness of narrow-band selection (when combined with further photometric information) in tracing the LSS at high redshift. This also shows that with modest spectroscopic observations ($\sim$ 1-2 hours), true high-z clusters can be efficiently confirmed. We also find some fillers and serendipitous detections with spectroscopic redshifts in the vicinity of the protocluster.

3.5. *Ancillary Spectroscopic Data*

In the vicinity of the protocluster (150.12 < RA (deg) < 150.28, +1.92 < Dec (deg) < +2.08, 2.21 < z < 2.25), we find 12 sources with spectroscopic redshift measurements from the zCOSMOS-deep survey (Lilly et al. in prep, also see Lilly et al. 2009). We consider these as potential cluster members in addition to our observations. In Table 1, we denote these extra sources by the label "ancillary".

4. PROTOCLUSTER CHARACTERISTICS

4.1. *Redshift and Velocity Dispersion*

To select the protocluster members, we first determine the mean redshift and standard deviation of all unique galaxies (primary, filler, serendipitous, ancillary). Sources that are within 3 standard deviation of the mean redshift are then used to determine the new mean redshift and standard deviation. We iteratively repeat this process until a final mean redshift (z_{mean}) and standard deviation (σ_z) is obtained. Only three galaxies (commented as "field" in Table 1) do not pass the selection criterion. With the remaining 47 galaxies (35 from our observation and 12 from ancillary data), we estimate the mean redshift, line-of-sight dispersion in redshift space, and line-of-sight velocity dispersion (σ_{los}=cσ_z/(1+z) where c is the speed of light) as z_{mean}=2.23224 $\pm$ 0.00101, σ_z= 0.00696 $\pm$ 0.00074, and

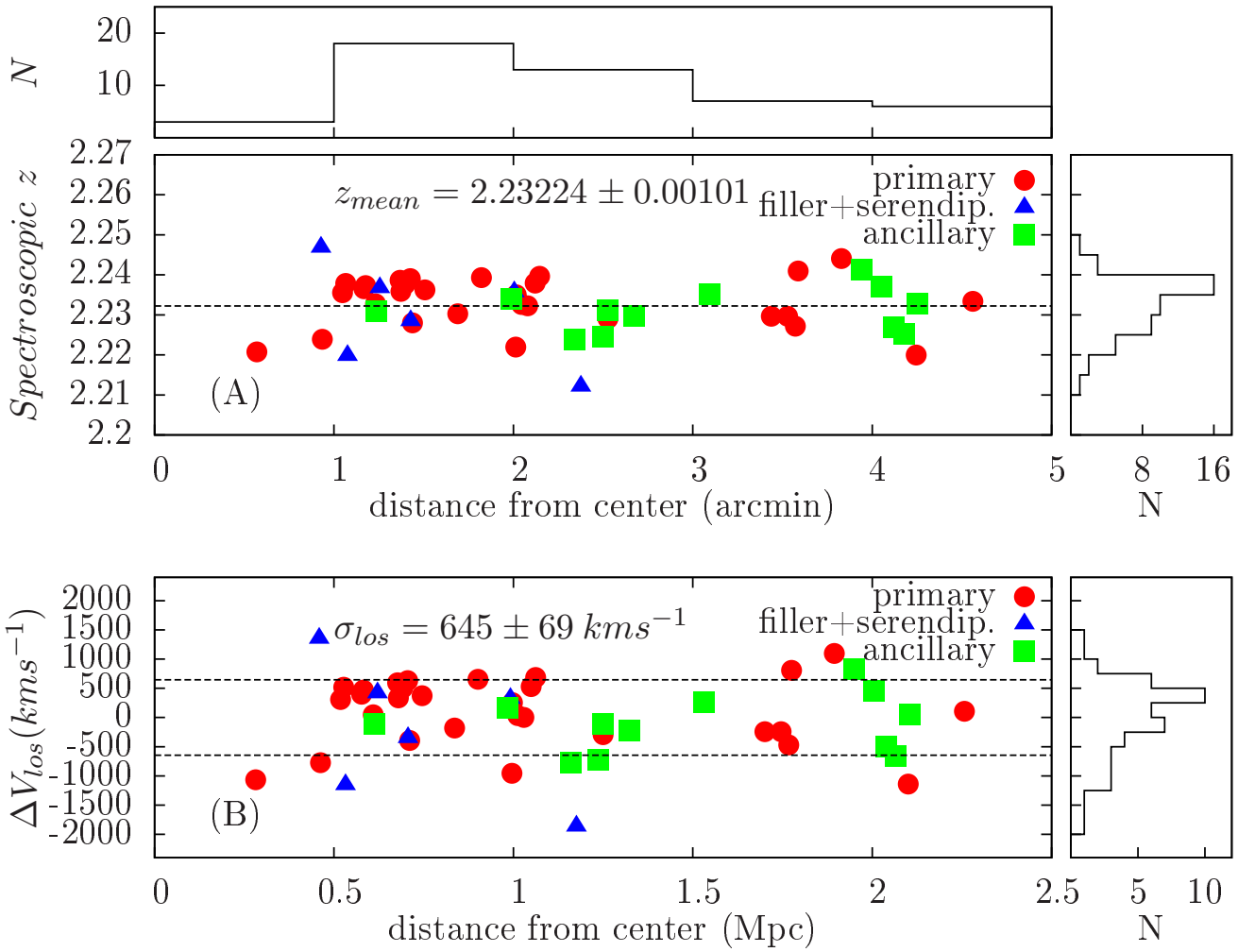

FIG. 3.— (A) Redshift distribution of confirmed members (circles are primaries, triangles are fillers and serendipitous sources) as a function of projected distance (in arcmin) from the center of the protocluster. z_{mean} of the protocluster is shown with a black dashed line. (B) line-of-sight velocity distribution with respect to the mean redshift as a function of projected distance (in Mpc) from the center. σ_{los} boundaries for the member galaxies are shown with black dashed lines.

σ_{los}=645 ± 69 km s^{-1}, respectively. The uncertainties are estimated using the bootstrap method with 10,000 resamples. If we only rely on the primary sources (29 galaxies), we obtain z_{mean}(primary)=2.23321 ± 0.00113, σ_z(primary)=0.00615 ± 0.00073, and σ_{los}(primary)=570 ± 67 km s^{-1}, consistent with measurements using all the galaxies.

To investigate the role of a small sample size on the results, following Yuan et al. (2014), we randomly select only 10 galaxies from our 47 members and recalculate the velocity dispersion. We estimate the new bootstrapped velocity dispersion as $\sigma_{los}(bootstrap)$=589 ± 149 km s^{-1}, consistent with what we found using the full sample, but with larger uncertainties. Figure 3 shows the redshift distribution, mean redshift, line-of-sight velocity distribution with respect to the mean redshift, and σ_{los} boundaries for our member galaxies.

4.2. *Spatial Distribution*

We consider the centroid of the selected protocluster members as the protocluster center at RA=150.197509 (deg) and Dec=+2.003213 (deg). The centroid is defined as the arithmetic mean of the Cartesian unit vectors representing the protocluster members. For a 2D Gaussian distribution, ∼ 40% of the weight of the distribution is within one standard deviation. Hence, we use the projected radius from the protocluster center that contains 40% of the members as a proxy for the typical radius of the core of the protocluster and estimate it to be R_{proj}=0.75 ± 0.11 Mpc. Using only primary sources, we obtain RA(primary)= 150.208397 (deg), Dec(primary)=+2.000796 (deg), and R_{proj}(primary)=0.65 ± 0.13 Mpc. Fig 4 (A) shows the spatial distribution of the members. In Fig 4 (B), they are color-coded by the line-of-sight velocities relative to the mean redshift of the protocluster. We find that 51(87)% of members are within 1(2) Mpc from the protocluster center.

The match to COSMOS2015 catalog shows that three of the members, mask1-1, mask1-15, and mask1-16 have *Chandra* X-ray detections (Elvis et al. 2009; Civano et al. 2016; Marchesi et al. 2016). This comprises 6.8±3.7% (6.9±4.9%) of the members (primary members), a factor of ∼ 4 larger than the overall fraction of X-ray detected Hα emitters in the HiZELS/COSMOS field at z=2.23 (Calhau et al. 2017). All three have broad emission lines, indicative of their AGN nature and they are all Lyα emitters as well (Matthee et al. 2016; Sobral et al. 2017). The

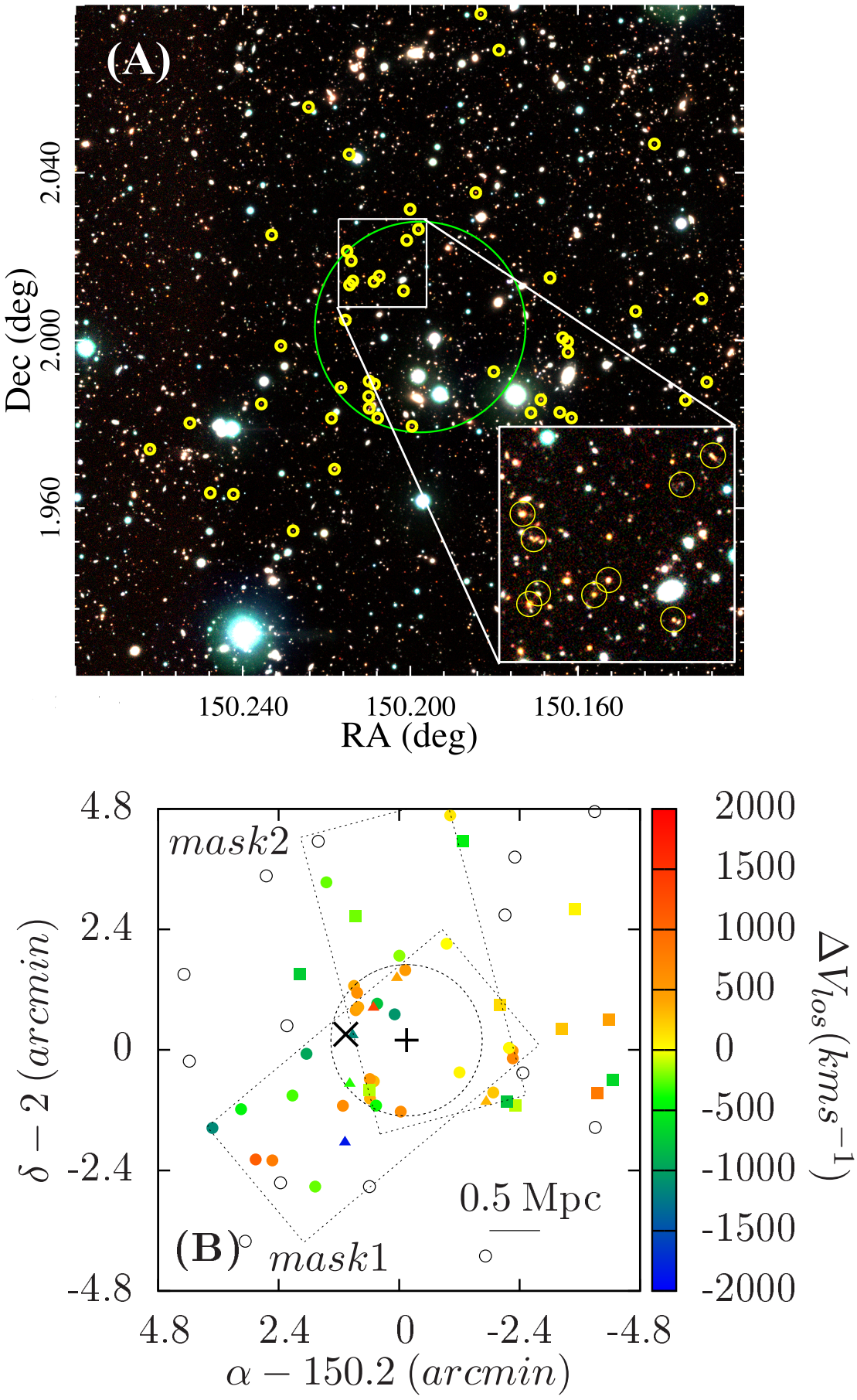

FIG. 4.— Top panel — (A) Three-color RGB image in the vicinity of the protocluster. Yellow circles show the spatial distribution of the members. The green circle corresponds to the R_{proj} of the protocluster. The red, green, and blue channels correspond to the UltraVISTA K_s, J, and Y bands, respectively (McCracken et al. 2012). Bottom panel — (B) Spatial distribution of the protocluster members (circles are primaries, triangles are fillers and serendipitous sources, and squares are ancillary sources) color-coded by their line-of-sight velocities with respect to the mean redshift. The primary sources not observed (here in this paper or as ancillary) are shown with empty circles. The positions of the spectroscopic masks are shown with dashed rectangles. The plus sign shows the protocluster center. The dashed circle shows the estimated R_{proj} of the protocluster. The multiplication sign shows the position of a candidate cluster (Rettura et al. in prep.) seen as an overdensity of *Spitzer*-detected galaxies, reinforcing the reality of the structure.

enhanced fraction of X-ray detected AGN in the protocluster relative to the field is in good agreement with Lehmer et al. (2013). mask1-16 also has a VLA 20 cm radio detection (Schinnerer et al. 2010). These indicate that highly rare and active systems, such as extreme X-ray sources and radio galaxies trace dense environments at high-z, further supporting the dense nature of the protocluster. A detailed analysis of the AGN fraction will be presented in a following paper.

4.3. *Dynamical Mass*

If we assume that the protocluster is virialized (see Section 4.4) and σ_{3d} and R_{proj} are the total velocity dispersion and characteristic radius of the protocluster's core, then we can estimate its virial mass from the virial theorem as M_{vir}=$R_{proj}\sigma_{3d}^2$/G, where G is the gravitational constant. Assuming a spherical symmetry, σ_{3d}^2=$3\sigma_{los}^2$. Substituting R_{proj} and σ_{los} into the equation gives M_{vir}=($3R_{proj}\sigma_{los}^2$/G)=$(2.2 \pm 0.6) \times 10^{14}$ $M_\odot$. With primary sources, we obtain M_{vir}(primary)=$(1.5 \pm 0.5)\times10^{14}$ $M_\odot$.

We can alternatively estimate the virial mass if we assume that the virial theorem applies to the protocluster and the halo of the protocluster is a spherical region within which the average density is $200\rho_c(z)$, where $\rho_c(z)$ is the critical density of the universe at redshift of z (Navarro et al. 1997). Then, we can express the virial mass (M_{200}) of the protocluster in terms of its virial radius r_{200} and the critical density as M_{200}=$\frac{4\pi}{3}r_{200}^3 200\rho_c(z)$. The critical density can be expressed in term of the Hubble parameter ($H(z)$) as $\rho_c(z)$=$3H^2(z)$/(8πG). Assuming a spherical symmetry combined with the virial theorem implies r_{200}=GM_{200}/($3\sigma_{los}^2$). Therefore, we can express r_{200} and M_{200} as functions of σ_{los} and $H(z)$ as r_{200}=$\sqrt{3}\sigma_{los}$/(10$H(z)$) and M_{200}=$(\sqrt{3}\sigma_{los})^3$/(10G$H(z)$) (Carlberg et al. 1997). We estimate r_{200}=0.49 $\pm$ 0.05 Mpc and M_{200}=$(1.4 \pm 0.5)\times10^{14}$ $M_\odot$. Using only primary sources, r_{200}(primary)=0.43 $\pm$ 0.05 Mpc and M_{200}(primary)=$(1.0 \pm 0.3)\times10^{14}$ $M_\odot$. These are in good agreement with R_{proj} and M_{vir} found above.

The *Spitzer* Archival Cluster Survey (SACS) is a comprehensive search for distant galaxy clusters in all *Spitzer*/IRAC extragalactic pointings available in the mission archive (Rettura et al. 2019 in prep.). Using the algorithm described in Rettura et al. (2014), high-redshift clusters are identified as overdensities in the mid-infrared data combined with shallow all-sky optical data. We find a match in their catalog (at a similar redshift) separated by only $\sim 1.2'$ from our protocluster. The position of their candidate is shown with a multiplication sign in Figure 4. This provides further confirmation for the existence of the detected structure as Rettura et al. use a completely independent approach in finding high-z protoclusters. Based on a relation calibrated in Rettura et al. (2018) (see their Eq. 6), they use the *Spitzer* 4.5 μm richness of their clusters to infer their dynamical mass. This candidate cluster has an estimated mass, $\log(M_{500}/M_\odot) = 14.06 \pm 0.25$, consistent with our estimate based on the velocity dispersion.

Using simulated clusters, Munari et al. (2013) suggest a scaling relation as $M_{200}/10^{15}M_\odot$=$(\sigma_{1D}/A_{1D})^{-\alpha}/h(z)$, where A_{1D} and α are two parameters, σ_{1D} is the 1D velocity dispersion, and $h(z) = H(z)/H_0$. According to their Figure 3, $A_{1D} \sim 1185 \pm 30$ km s^{-1} and $\alpha \sim 0.38 \pm 0.01$ at z=2 using galaxies as a tracer for the total mass of clusters. With this scaling relation, we obtain M_{200}(scaling)=$(3.8 \pm 0.2)\times10^{14}$ $M_\odot$, a factor of ~ 3 larger than M_{200} we found before but within the same order of magnitude.

We note that we have made a number of assumptions, such as virialization and the spherical symmetry in estimating the dynamical quantities. These assumptions may not be entirely correct, particularly for protoclusters at high redshift as they are likely still forming (see Section 4.4). Therefore, these should be considered as order-of-magnitude estimates of the protocluster mass. In table 2, we summarize the protocluster characteristics using all the members and primary sources only.

TABLE 2
Protocluster Characteristics

quantity	all members	primary members only
RA(deg)	150.197509	150.208397
Dec(deg)	+2.003213	+2.000796
z_{mean}	2.23224±0.00101	2.23321±0.00113
σ_{los}(km s^{-1})	645±69	570±67
R_{proj}(Mpc)	0.75±0.11	0.65±0.13
$M_{vir}(10^{14}$ $M_\odot)$	2.2±0.6	1.5±0.5
r_{200}(Mpc)	0.49±0.05	0.43±0.05
$M_{200}(10^{14}$ $M_\odot)$	1.4±0.5	1.0±0.3

4.4. *Protocluster's Fate*

Is the protocluster relaxed and fully virialized by the time of observation ($z \sim 2.23$)? The redshift distribution is not symmetrically Gaussian (skewness=-0.5262, although the difference from a normal distribution is at $< 1.6\ \sigma$ significance level) and the line-of-sight velocities with respect to the mean redshift are not fully symmetric (Figure 3), indicating that the structure is still in the assembly process. As shown in Figure 1, the presence of other potential overdensities and filamentary-like structures in the vicinity of the protocluster further suggests that the structure is likely not relaxed at $z \sim 2.23$ and still coalescing.

We estimate the dynamical timescale (τ_{dyn}) of the protocluster. The protocluster could be virialized at $z \sim 2.23$ if at least one dynamical timescale (in practice, a few) has elapsed since its formation. We estimate $\tau_{dyn} \sim r_{3d}/\sigma_{3d}$ where r_{3d} is the characteristic radius of the protocluster and σ_{3d} is its total velocity dispersion. If we assume $r_{3d} \sim R_{proj}$ and the spherical symmetry and use the estimated line-of-sight velocity dispersion and R_{proj} from Section 4.1, we obtain $\tau_{dyn} \sim 0.75$ Mpc/($\sqrt{3}$ $\times$645 km s^{-1}) ~ 0.6 Gyr. Therefore, if the protocluster was initially formed prior to $z \sim 2.8$, it would have had sufficient time to get virialized by the time of observation. Estimating the formation epoch of the protocluster is not straightforward. However, the average age of the stellar populations of its member galaxies, particularly the quiescent systems can place robust constraints on its formation time. By selection, quiescent galaxies are currently

missing in our spectroscopic observation. However, future deep follow-up spectroscopic observations of potential passive galaxies in the protocluster can put stringent constraints on its formation epoch.

Is the protocluster relaxed by now (z=0)? To answer this, we investigate the evolution of the protocluster overdensity in the linear regime of a spherical collapse model and compare it with the critical collapse threshold of δ_c=1.69 [9]. Within a redshift slice of $\Delta z \sim 0.03$ (width of the narrow-band filter) and a projected 2 Mpc radius circle placed at the center of the protocluster, we find 35 Hα emitters (the original sample from which the primary targets were selected for spectroscopy). The average number of Hα emitters in the same volume is $\sim$ 4.6 (corrected for the effective area of the survey and the enhancement due to the overdensity). Therefore, using narrow-band selected Hα emitters, the galaxy number density enhancement is δ_g=$\frac{35-4.6}{4.6}$=6.6.

Following Steidel et al. (2005), δ_g is related to the mass density enhancement (δ_m) via 1+bδ_m=C(1+δ_g), where b is the clustering bias and C is a correction term due to the redshift space distortions and is calculated using C=1+f-f(1+δ_m)$^{1/3}$, where f=$\Omega_m(z)^{0.6}$. Using f(z=2.23)=0.96 and the clustering bias of b=2.4 for the Hα emitters at $z \sim 2.23$ (Geach et al. 2012), we obtain δ_m(z=2.23) $\sim$ 1.61. In a spherical collapse model (Mo & White 1996), this is related to a linear matter enhancement of δ_L(z=2.23) $\sim$ 0.73 and is expected to grow to δ_L(z=0) $\sim$ 1.9 by z=0. This exceeds the collapse threshold of δ_c=1.69. Therefore, the protocluster is expected to fully collapse and virialize by now (z=0). In fact, the linear matter enhancement reaches the collapse threshold at $z \sim 0.1$, indicating that the protocluster should have been virialized since the past $\sim$ 1.0-1.5 Gyr. The collapse threshold at any redshift is approximated as $\delta_c(z) \simeq 1.69D(z{=}0)/D(z)$, where $D(z)$ is the linear growth function (Percival 2005). At the redshift of the protocluster, $\delta_c(z = 2.23) \sim 4.3$. This is larger than δ_L(z=2.23), further inidcating that the structure is likely not virialized at z=2.23.

We estimate the virialized mass of the protocluster at present $M_{dyn}(z{=}0)$ through $M_{dyn}(z{=}0) = \rho_m(V_{obs}/C)(1{+}\delta_m)$, where ρ_m is the mean comoving density, V_{obs} is the observed comoving volume of the structure, and C is the correction term introduced above (Steidel et al. 1998). The Hα emitter candidates are dominated by those selected in UKIRT/WFCAM narrow-band K filter (Sobral et al. 2013). Assuming a tophat shape for the filter corresponds to a redshift width of $\Delta z \sim 0.032$ centered at $z \sim 2.23$. The corresponding comoving radial width ($\Delta\chi$) is then $\sim$ 42 Mpc. This leads to the comoving $V_{obs} \sim 5500$ Mpc^3 for a cylinder of width $\Delta\chi$ and a projected physical radius of 2 Mpc at $z \sim 2.23$. Given δ_m(z=2.23) $\sim$ 1.61 and C=0.64, we estimate $M_{dyn}(z{=}0) \sim 9.2{\times}10^{14}$ $M_\odot$. Therefore, the protocluster is likely the progenitor of a Coma-type cluster at z=0. Simulations of Chiang et al. (2013) show that at $z > 2$, the progenitors of a Coma-type cluster traced by SFR > 1 $M_\odot$yr^{-1} galaxies are expected to have a galaxy density enhancement of $\delta_g \sim 5.5^{1.5}_{-0.8}$ probed over $15^3 \sim 3500$ Mpc^3 comoving volumes. These values are in rough agreement with our measurements, indicating that our protocluster is expected to evolve into a $\sim 10^{15}$ $M_\odot$ Coma-type cluster at z=0.

The comoving volume associated with Hα emitter candidates in the HiZELS/COSMOS field is $\sim 5.48 \times 10^5$ Mpc^3 (Sobral et al. 2013). Given the detection of one protocluster in this volume, we estimate a comoving space and mass density of $\sim 1.8 \times 10^{-6}$ Mpc^{-3} and $\sim (1.8-3.6){\times}10^8$ $M_\odot$ Mpc^{-3} for a $M_{dyn} \sim (1-2){\times}10^{14}$ $M_\odot$ protocluster at $z \sim 2$. However, we note that Poisson uncertainties are as large as the reported values. With the Poisson uncertainty, the space density of the protocluster is $\lesssim 3.6 \times 10^{-6}$ Mpc^{-3}. The halo mass function of Bocquet et al. (2016) predicts a space density of $\sim$ 1-2 $\times 10^{-7}$ Mpc^{-3} for a $M_{200} \sim 10^{14}$ $M_\odot$ halo at z=2, a factor of $\sim$ 10 smaller than our estimate, but consistent with it given the large Poisson uncertainty in our measurement. Moreover, for a sample of similarly selected Hα emitters in the UDS (Sobral et al. 2013) and Boötes (Matthee et al. 2017) fields at $z \sim 2.2$ with comoving volumes of $\sim 2.24 \times 10^5$ Mpc^3 and $\sim 2.7 \times 10^5$ Mpc^3, respectively, no overdensity of Hα emitters is found. This increases the effective volume and subsequently decreases the space density of our protocluster, making our measurement more consistent with the halo mass function predictions.

5. COMPARISON

We compare the present-day mass of $z \gtrsim 1.5$ protoclusters compilation from Overzier (2016) with that of our protocluster. The median protocluster in the compilation has a present-day mass of $\log(M(z=0)/M_\odot)$=14.6. This makes our protocluster one of the most massive systems with a z=0 mass comparable to some remarkable high-z protoclusters with $M(z{=}0) \gtrsim 10^{15}$ $M_\odot$ (Venemans et al. 2002; Cucciati et al. 2014; Lemaux et al. 2014; Lee et al. 2014; Diener et al. 2015; Bădescu et al. 2017; Oteo et al. 2018; Chanchaiworawit et al. 2019).

Protoclusters at $z \sim$ 2-3 in the Overzier (2016) compilation have galaxy overdensities in the range $\delta_g \approx$ 1.5-16, with those that used Hα emitters as the tracer of overdensity have $\delta_g \approx$ 4-16. We note that these values are measured differently with different selection functions and volumes probed. Therefore, these should not be directly compared with one another and our work. Nevertheless, they show that our protocluster overdensity of $\delta_g \sim 7$ is typical of high-z protoclusters and they are in broad agreement with simulations of Chiang et al. (2013).

Cucciati et al. (2018) recently identified a super-protocluster in formation in the COSMOS field at $z \sim$ 2.45, dubbed "Hyperion", containing at least seven density peaks with masses in the range $\sim$ (0.1-2.7)$\times 10^{14}$ $M_\odot$. Hyperion is extended over a comoving volume of $\sim 60{\times}60{\times}150$ Mpc^3 and has an estimated total mass of $\sim 4.8{\times}10^{15}$ $M_\odot$. Could the extended LSS shown in Figure 1 (A) be a super-protocluster similar to "Hyperion"? The comoving radial distance between the northern cluster at $z \sim 2.1$ and our protocluster in the south is $\sim$ 180 Mpc. If the extended structure (including the central overdensity shown with a question mark and other potential surrounding overdensities) is confirmed to be a

[9] We note that this value of linearly-extrapolated critical density enhancement is for an Einstein-de Sitter cosmology. However, it has been shown to have a weak dependence on cosmological models (Percival 2005).

multi-component super-protocluster, it would have a comoving volume of $\sim 40\times40\times180$ Mpc^3, making it comparable to Hyperion. Follow-up spectroscopic observations could further reveal the nature of this structure.

6. SUMMARY

We report the spectroscopic confirmation of a new protocluster in the COSMOS field at z=2.23224 using Keck/MOSFIRE observations in combination with ancillary data from zCOSMOS-deep spectroscopic survey. With 47 confirmed members (35 from our MOSFIRE observations and 12 from ancillary data), we estimate a line-of-sight velocity dispersion and a total mass of σ_{los}=645 $\pm$ 69 km s^{-1} and $M_{dyn} \sim (1-2)\times10^{14}$ $M_\odot$ for the protocluster, respectively. The structure is likely not fully virialized at $z \sim 2.23$ but is expected to collapse to a Coma-type cluster with $M_{dyn}(z{=}0) \sim 9.2\times10^{14}$ $M_\odot$ at z=0.

With the high-quality data obtained, in forthcoming papers, we will investigate the role of early environments on the SFR (Hα or Hβ), nebular extinction (Hβ and Hα), gas-phase metallicity ([NII]λ6549, [NII]λ6583, and Hα), electron density ([SII]$\lambda\lambda$6717,6731 doublet), source of ionization (BPT diagram), ionization state of the gas ([OIII]λ4959, [OIII]λ5007, and Hβ), mergers, dynamics, and AGN fraction relative to galaxies in the field. Moreover, follow-up spectroscopy can further reveal the potential multi-component nature of the structure shown in Figure 1.

ACKNOWLEDGEMENTS

B.D. acknowledges financial support from NASA through the Astrophysics Data Analysis Program (ADAP), grant number NNX12AE20G, and the National Science Foundation, grant number 1716907. B.D. is thankful to Andreas Faisst, Laura Danly, and Matthew Burlando for their companionship during the observing run. B.D. is grateful to the COSMOS team for their useful comments during the team meeting in New York City 14-17 May 2019. The observations presented herein were obtained at the W. M. Keck Observatory (program C236, PI Scoville), which is operated as a scientific partnership among the California Institute of Technology, the University of California, and the National Aeronautics and Space Administration. The Observatory was made possible by the generous financial support of the W. M. Keck Foundation. The authors would like to recognize and acknowledge the very prominent cultural role and reverence that the summit of Mauna Kea has always had within the indigenous Hawaiian community. We are fortunate to have the opportunity to perform observations from this mountain.

REFERENCES

Bocquet, S., Saro, A., Dolag, K., & Mohr, J. J. 2016, MNRAS, 456, 2361
Bădescu, T., Yang, Y., Bertoldi, F., et al. 2017, ApJ, 845, 172
Calhau, J., Sobral, D., Stroe, A., et al. 2017, MNRAS, 464, 303
Capak, P. L., Riechers, D., Scoville, N. Z., et al. 2011, Nature, 470, 233
Carlberg, R. G., Yee, H. K. C., Ellingson, E., et al. 1997, ApJL, 485, L13
Chanchaiworawit, K., Guzmán, R., Salvador-Solé, E., et al. 2019, ApJ, 877, 51
Chiang, Y.-K., Overzier, R., & Gebhardt, K. 2013, ApJ, 779, 127
Chiang, Y.-K., Overzier, R. A., Gebhardt, K., et al. 2015, ApJ, 808, 37
Civano, F., Marchesi, S., Comastri, A., et al. 2016, ApJ, 819, 62
Clements, D. L., Braglia, F. G., Hyde, A. K., et al. 2014, MNRAS, 439, 1193
Cucciati, O., Zamorani, G., Lemaux, B. C., et al. 2014, A&A, 570, A16
Cucciati, O., Lemaux, B. C., Zamorani, G., et al. 2018, A&A, 619, A49
Darvish, B., Mobasher, B., Martin, D. C., et al. 2017, ApJ, 837, 16
Darvish, B., Mobasher, B., Sobral, D., et al. 2016, ApJ, 825, 113
Darvish, B., Mobasher, B., Sobral, D., Scoville, N., & Aragon-Calvo, M. 2015, ApJ, 805, 121
Darvish, B., Scoville, N. Z., Martin, C., et al. 2018, ApJ, 860, 111
Diener, C., Lilly, S. J., Ledoux, C., et al. 2015, ApJ, 802, 31
Elvis, M., Civano, F., Vignali, C., et al. 2009, ApJS, 184, 158
Geach, J. E., Sobral, D., Hickox, R. C., et al. 2012, MNRAS, 426, 679
Hayashi, M., Tadaki, K.-i., Kodama, T., et al. 2018, ApJ, 856, 118
Horne, K. 1986, PASP, 98, 609
Ilbert, O., Capak, P., Salvato, M., et al. 2009, ApJ, 690, 1236
Ilbert, O., McCracken, H. J., Le Fèvre, O., et al. 2013, A&A, 556, A55
Kacprzak, G. G., Yuan, T., Nanayakkara, T., et al. 2015, ApJL, 802, L26
Khostovan, A. A., Sobral, D., Mobasher, B., et al. 2015, MNRAS, 452, 3948
Koyama, Y., Kodama, T., Tadaki, K.-i., et al. 2013, MNRAS, 428, 1551
Laigle, C., McCracken, H. J., Ilbert, O., et al. 2016, ApJS, 224, 24
Lee, K.-S., Dey, A., Hong, S., et al. 2014, ApJ, 796, 126
Lee, M. M., Tanaka, I., Kawabe, R., et al. 2017, ApJ, 842, 55
Lehmer, B. D., Lucy, A. B., Alexander, D. M., et al. 2013, ApJ, 765, 87
Lemaux, B. C., Cucciati, O., Tasca, L. A. M., et al. 2014, A&A, 572, A41
Lemaux, B. C., Le Fèvre, O., Cucciati, O., et al. 2018, A&A, 615, A77
Lilly, S. J., Le Brun, V., Maier, C., et al. 2009, ApJS, 184, 218
Madau, P., & Dickinson, M. 2014, ARAA, 52, 415
Marchesi, S., Civano, F., Elvis, M., et al. 2016, ApJ, 817, 34
Matsuda, Y., Yamada, T., Hayashino, T., et al. 2004, AJ, 128, 569
Matsuda, Y., Smail, I., Geach, J. E., et al. 2011, MNRAS, 416, 2041
Matthee, J., Sobral, D., Best, P., et al. 2017, MNRAS, 471, 629
Matthee, J., Sobral, D., Oteo, I., et al. 2016, MNRAS, 458, 449
McCracken, H. J., Milvang-Jensen, B., Dunlop, J., et al. 2012, A&A, 544, A156
Mo, H. J., & White, S. D. M. 1996, MNRAS, 282, 347
Munari, E., Biviano, A., Borgani, S., Murante, G., & Fabjan, D. 2013, MNRAS, 430, 2638
Muzzin, A., Wilson, G., Demarco, R., et al. 2013, ApJ, 767, 39
Navarro, J. F., Frenk, C. S., & White, S. D. M. 1997, ApJ, 490, 493
Noble, A. G., McDonald, M., Muzzin, A., et al. 2017, ApJL, 842, L21
Oteo, I., Ivison, R. J., Dunne, L., et al. 2018, ApJ, 856, 72
Overzier, R. A. 2016, A&A Rev., 24, 14
Percival, W. J. 2005, A&A, 443, 819
Rettura, A., Chary, R., Krick, J., & Ettori, S. 2018, ApJ, 867, 12
Rettura, A., Martinez-Manso, J., Stern, D., et al. 2014, ApJ, 797, 109
Schinnerer, E., Sargent, M. T., Bondi, M., et al. 2010, ApJS, 188, 384
Scoville, N., Aussel, H., Brusa, M., et al. 2007, ApJS, 172, 1
Shimakawa, R., Kodama, T., Tadaki, K.-i., et al. 2015, MNRAS, 448, 666
Shimakawa, R., Kodama, T., Hayashi, M., et al. 2018, MNRAS, 473, 1977
Sobral, D., Best, P. N., Smail, I., et al. 2014, MNRAS, 437, 3516
Sobral, D., Smail, I., Best, P. N., et al. 2013, MNRAS, 428, 1128
Sobral, D., Matthee, J., Best, P., et al. 2017, MNRAS, 466, 1242

Steidel, C. C., Adelberger, K. L., Dickinson, M., et al. 1998, ApJ, 492, 428
Steidel, C. C., Adelberger, K. L., Shapley, A. E., et al. 2005, ApJ, 626, 44
Strazzullo, V., Daddi, E., Gobat, R., et al. 2015, A&A, 576, L6
Valentino, F., Daddi, E., Strazzullo, V., et al. 2015, ApJ, 801, 132
Venemans, B. P., Kurk, J. D., Miley, G. K., et al. 2002, ApJL, 569, L11
Venemans, B. P., Röttgering, H. J. A., Miley, G. K., et al. 2007, A&A, 461, 823
Wylezalek, D., Galametz, A., Stern, D., et al. 2013, ApJ, 769, 79
Yuan, T., Nanayakkara, T., Kacprzak, G. G., et al. 2014, ApJL, 795, L20